



science.sciencemag.org/cgi/content/full/science.aaw6888/DC1

Supplementary Materials for **Searching for hidden earthquakes in Southern California**

Zachary E. Ross*, Daniel T. Trugman, Egill Hauksson, Peter M. Shearer

*Corresponding author. Email: zross@gps.caltech.edu

Published 18 April 2019 on *Science* First Release
DOI: [10.1126/science.aaw6888](https://doi.org/10.1126/science.aaw6888)

This PDF file includes:

Materials and Methods
Supplementary Text
Figs. S1 to S9
References

Materials and Methods

Data

In this study, we used continuous seismic data collected by the Southern California Seismic Network (SCSN) over the period 2008-2017. All available stations with EH and HH channels were used. The station membership of the SCSN evolved over time, but in total 513 unique stations were used at one point or another (Fig. S4). We filtered the waveform data with a Butterworth filter between 2-15 Hz and downsampled to 50 Hz for computational efficiency. The dataset was organized into 24-hour continuous files with all gaps filled with zeros.

Template events were taken from the standard seismicity catalog produced by the SCSN. All local earthquakes listed in the catalog from 2000-2017 were preliminarily selected as template events, which total 284,149. We note that the template events start from the year 2000, rather than 2008 like the continuous data, because triggered waveforms exist further back in time but can still be used for the analysis. Template waveforms were then constructed for all stations with phase picks made by the SCSN, and were filtered and downsampled in an identical manner to the continuous data. The phase picks have all been manually reviewed by professional seismic analysts. P-wave templates were 2.5 seconds long or equal to the S-P time (whichever was shorter), whereas S-wave templates were 4.0 seconds long. Template waveforms were chosen to start 0.5 seconds before the phase arrival time. P-wave template waveforms were only taken from vertical components, while S-wave template waveforms were taken from horizontal components. We limited the maximum source-receiver distance of template waveforms to 50 km, a compromise between maximizing detection sensitivity and missing events entirely in the coarsest parts of the network.

Template matching

The template matching procedure is a modified version of the technique developed by Shelly et al. (8). For each day of continuous data in the study period, each of the template events was used to calculate cross-correlation functions. For a given template event, each of the available template waveforms was then checked to ensure the signal to noise ratio was above 5.0, using a 4-second long window prior to the P-wave onset as the noise window, and any template waveforms for which this criterion was not met were discarded. We then required a minimum of 12 template waveforms to proceed, or else the template event was discarded altogether. Since there is a maximum of 1 P-wave and 2 S-wave templates per station, this translates into a minimum of 4 stations needed to run a template event.

Next, the template waveforms were cross-correlated against 24 hours of continuous data resulting in correlation functions that were nearly 24 hours in duration. Correlations were only performed for templates and continuous data with identical station and channel codes. These correlation functions were then migrated back in time by the observed travel time of the matching template waveform, as defined by the time difference between the analyst pick and the origin time. The migration operation resulted in a time series in 'origin time space'. Then, these migrated correlation functions were stacked over all stations, channels, and phases. The median absolute deviation was calculated for the stacked correlation function, and an initial detection threshold was set at 9.5 median absolute deviations. This threshold was chosen based on visual examination of thousands of detections. The time corresponding to the peak correlation value for each trigger was taken as the origin time of the detected event.

The initial list of detections made by the template event was then subjected to additional post-processing steps for quality control purposes. First, to remove any cases where duplicate detections of the same event may have occurred, we merged together detections separated less than 2.0 seconds apart, and the detection with the largest stacked correlation coefficient was taken as the final detection. At this point, an initial location was assigned to the detection that was equal to the hypocenter of the template event.

All of the processing steps listed above pertain to a single template event. The entire methodology is repeated for all template events in the set, for all of the days of data. Due to the potential for multiple template events to detect the same event, duplicates were identified as events separated by less than 2.0 seconds, and the detection with the largest cross-correlation coefficient was chosen as the final detection. Detections are generally very closely located to the template events that detected them, since the waveforms are required not only to be highly similar but have precisely the same moveout. This generally limits detections to within ~100-200m. However, due to random chance, events will occasionally be detected by templates that are much further away. This is the reason for imposing a minimum separation time of 2.0 sec: so that duplicate detections are minimized.

We used an array of 200 NVIDIA P100 GPUs to perform the cross-correlations, in an effort that totaled roughly 300,000 GPU hours and more than one million CPU hours over several iterations. Then, we performed a search across the set of detections to identify which were re-detections of the template events themselves. There are various conditions for which a template event might not be recovered by the detection process, including an insufficient number of channels meeting the SNR criteria or phase criteria. For these reasons, these missing template events were added back to the catalog to ensure that it was an exact superset of the SCSN catalog. The entire procedure resulted in a set of 1,811,362 detections.

Catalog quality control and false alarms

The QTM catalog is a fully automated seismicity catalog, with the exception of the template events that were taken from the SCSN catalog. We examined thousands of detections randomly to determine the optimal detection thresholds and the approximate false alarm rates that these thresholds correspond to. The base QTM catalog, which contains 1.81 million earthquakes, used a threshold of 9.5 median absolute deviations, and has an approximate false alarm rate of 5%. We also provide an even higher quality catalog, using a threshold of 12 median absolute deviations, which has 853,764 earthquakes (4.74 times increase), and has a false alarm rate of less than 1%.

Magnitude estimation

We determined magnitudes using an approach based on amplitude ratios between the newly detected events and the template events. For each template waveform and the matching detection waveform, we calculated the peak amplitudes and corrected them for any differences in gain factors. Then the amplitude ratio was formed and translated into a magnitude difference by taking its logarithm and assuming a factor of 10 difference in amplitude was equal to a unit difference in magnitude.

One strategy at this point is to take the average or median of the logarithmic amplitude ratios and add this to the magnitude of the template event. We found that for most events, this performed well, but for a few percent of the events, the magnitudes were slightly biased due to the inclusion of too many noisy amplitudes from operating so close to the ambient noise level.

Furthermore, it is desirable to provide realistic estimates of the errors in the magnitudes. Therefore, we performed a Bayesian estimation (35) of the magnitude, by calculating the posterior distribution,

$$p(M | d) = L(d|M)p(M),$$

where d represents the observations (here, these are the set of logarithmic amplitude ratios) and M is magnitude. The prior $p(M)$ is given by,

$$p(M) = \begin{cases} K 10^{-M}, & \text{if } M_l \leq M \leq M_h, \\ 0, & \text{otherwise} \end{cases}$$

where K is a normalization constant and M_l, M_h represent truncation limits to the exponential. Here, we use $M_l = -2$, reflecting the limit to which we expect to detect earthquakes on the low end, and set M_h equal to the magnitude of the template event associated with each detection, since we do not anticipate detecting larger earthquakes that do not already appear in the SCSN catalog. For the likelihood function, $L(d|M)$, we use the Laplace distribution, which is an exponential where the errors follow an L1 norm,

$$L(d|M) = \prod_i \frac{1}{2b} e^{-|M-d_i|/b}.$$

The Laplace distribution was chosen instead of the more commonly selected Gaussian (and associated L2 norm), since it is more robust in the presence of statistical outliers, which are pervasive in large earthquake datasets. The Laplacian scale parameter, b , was chosen to be 0.33 based on inspection of the scatter for numerous events' amplitude ratios. For our catalog, we report three values taken from the posterior distribution: the median, the 5th percentile, and the 95th percentile, which can be used to define a magnitude and a credibility interval.

Magnitude of completeness estimation

We used the Goodness-of-Fit (GFT) technique (36) to assess the magnitude of completeness M_c of the QTM catalog, while acknowledging that a single summary statistic like M_c masks the large spatiotemporal variability inherent to the dataset. In brief, the GFT technique interprets M_c as the magnitude above which the cumulative magnitude distribution can be interpreted as a Gutenberg-Richter power law. Rather than preselect a threshold value of goodness-of-fit (a practice which can sometimes produce unstable results (37)), we instead select the M_c value as point at which the goodness-of-fit vs. M_c curve begins to level off. With this approach, the estimated M_c values for the QTM and the 2008-2017 subset of the SCSN catalog are 0.3 and 1.7, respectively (Figure S5).

For comparison, we also show the M_c estimates obtained from the maximum curvature (MAXC) technique, which interprets M_c as the peak of the incremental magnitude distribution. The GFT estimates are 0.5-0.6 M units larger than the MAXC estimates, which is expected given the tendency for MAXC to underestimate the true M_c (37). We also note that the maximum likelihood estimate for the Gutenberg-Richter b -value (38) for our study region is relatively low, of order 0.8 for both the QTM and SCSN catalogs. This likely reflects the high seismicity rate in Baja California (especially in the aftermath of the 2010 M7.2 El Mayor-Cucapah earthquake), where SCSN network coverage is limited. Within the heart of the network (Figure S4), b -values are in the range 0.9-1.0.

Seismicity relocation

Next, we relocated all template events individually using a 3D velocity model (17, 39). Then, for each earthquake in the catalog, including template events, we determined the 200 nearest

neighbor template events to be used for pairwise cross-correlation to measure differential times. For each event pair, we prepared data windows that were 1.0 sec long for P-waves and 1.5 sec long for S-waves, starting 0.25 sec before a given phase arrival. Phase picks were made by analysts at the SCSN and have all been manually reviewed. The maximum source-receiver distance allowed was 100 km. We required at least 6 differential times with a cross-correlation coefficient of 0.6 or greater in order to save the values for an event pair. This process resulted in ~1.63 billion differential times and 99.4 million event pairs.

We then refine the location precision of the catalog using GrowClust (16), a cluster-based relative relocation technique. GrowClust applies agglomerative, hierarchical clustering to differential travel time data for pairs of earthquakes observed at a set of common stations. The clustering algorithm uses a robust, L1-norm approach to define the relative hypocentral positions that are most consistent with the observed set of differential times. While the GrowClust algorithm is designed to scale to large datasets, the unprecedented size and unique structure of the QTM catalog required several preprocessing steps, which we describe below.

The locations of the detected events are unknown a priori, though they are likely to be in the neighborhood of the source region of the detecting template in order to produce high waveform similarity. We thus set the initial location of each detected event to the location of its associated template event. We take advantage of the fact that the template event locations are significantly better resolved than detected event locations by rescaling the GrowClust waveform similarity coefficients by a factor of 100 for template-template event pairs, relative to the similarity coefficients of the template-detection event pairs. This ensures that the template events are relocated first with respect to one another during the GrowClust algorithm clustering hierarchy, before relocating any of the detected events. This improves the final location accuracy of both the template and detected events, and also improves the GrowClust algorithm efficiency.

Since the full QTM catalog and the associated differential times are too large to fit into computer memory at once, we subdivided the full catalog into a set of 12 polygons, each with between 90,000 and 250,000 events (Figure S6). The polygon locations were determined automatically by applying a spectral clustering algorithm (40) to the template locations, a technique which groups events into clusters based on spatial connectedness and avoids subdividing the dataset in regions of dense seismicity (to the extent possible). To further mitigate the potential for edge artifacts, all polygon boundaries were padded with the 200 nearest neighbors of each event assigned to a given polygon. Detected events were assigned to the polygon of their associated template.

We prepared region-specific input files for each of these 12 polygons and used an MPI script to run GrowClust in parallel, with a total runtime in CPU hours of 18.84 for the optimal run parameters. We performed sensitivity analysis on the GrowClust run parameters, and found only minor variations in catalog quality by perturbing the default values. Overall, the best results were produced by setting $rmin = 0.65$, $ngoodmin = 8$, $rmsmax = 0.2$, $distmax1 = 5$, $distmax2 = 3$, $hshiftmax = vshiftmax = 1.5$, and $nclustmin = 1$ (see (16) and the associated User Guide for detailed descriptions of these parameters). In total, 701,262 of the events were able to be relocated, which is 38.7%. The Gutenberg-Richter statistics for these events are shown in Fig. 1. The minor discrepancy between the relocated and unrelocated events at $M > 3$ reflects a small number of larger events that were not successfully relocated (larger earthquakes tend to have unique waveforms that are dissimilar to other nearby events and hence do not cross-correlate well).

Static stress calculations

We used the Coulomb3 software package (41) to calculate the approximate change in static stress for the 2010 M7.2 El Mayor-Cucapah earthquake. Our simplified model of the El-Mayor-Cucapah earthquake emulates the fault orientation of previous source inversion solutions (27, 42), and assumes a planar rupture with constant slip, a rupture length $L = 75\text{km}$, rupture $W = 16\text{ km}$, *strike* = 319 degrees, *dip* = 77 degrees, and *rake* = -147 degrees. We calculated Coulomb stress change at 10km depth for aftershock fault planes aligned with the mainshock rupture (Figure S7). While the exact values are sensitive to the spatial stress patterns, assumed fault orientations, and other approximations inherent to Coulomb stress theory, the basic distance decay of static stresses are relatively insensitive to these assumptions. These calculations suggest that static stresses from the El Mayor-Cucapah event should be negligible to first order ($< 1\text{ kPa}$) at the greater distances where measurable triggering is observed in the QTM catalog. We note that these calculations are strictly due to the coseismic displacements and ignore the effect of any postseismic deformation and of dynamic triggering.

Future template matching catalogs for other seismic networks

We will provide the QTMATCH code for others to use for building template matching catalogs. The requirements for such catalogs are generally two-fold: a high-quality seismicity catalog and set of associated phase picks, and high-quality three-component continuous waveform datasets. While vertical only sensors can work, the S-waves are much weaker and often contribute more to the detection sensitivity than P-waves with lower energy. Station density generally is dependent on the targeted scale involved.

Supplementary Text

Catalog description

The QTM catalog will be publicly available through the Southern California Earthquake Data Center <scedc.caltech.edu>, along with all of the differential times and associated meta-data. The catalog is a superset of the SCSN catalog for the period 2008-2017. Each event is given a quality grade, where a quality of 1 indicates that an event has been manually reviewed by a professional seismic analyst at the SCSN; these events are those listed in the SCSN catalog. Of the newly detected events, the highest confidence detections are given a quality of 2. These detections correspond to a detection threshold of $12 \cdot \text{MAD}$ (see methods). The remainder of the detections are given a quality of 3, which corresponds to a detection threshold of $9.5 \cdot \text{MAD}$. Depending on the level of confidence necessary for a particular analysis, it is therefore possible to subset the catalog accordingly. We emphasize that events with quality 2 and 3 quality have not been manually reviewed. For those interested in experimenting with different detection thresholds, all of the necessary information is provided.

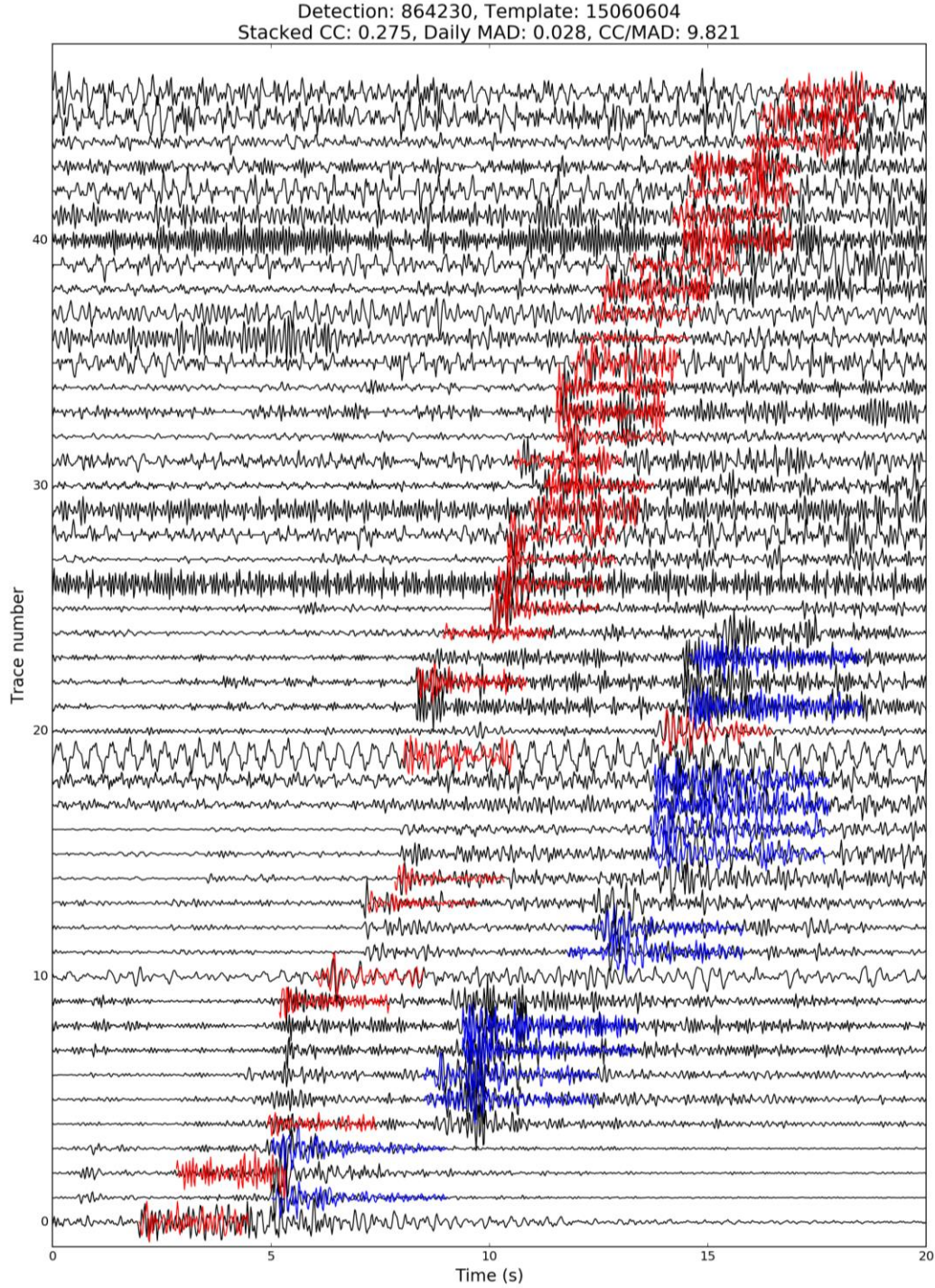


Fig. S1.

Example of an event detected with template matching. P-wave template waveforms are colored red, and S-wave template waveforms are colored blue. Note that not all stations have P and S template waveforms that meet the quality control criteria (Methods).

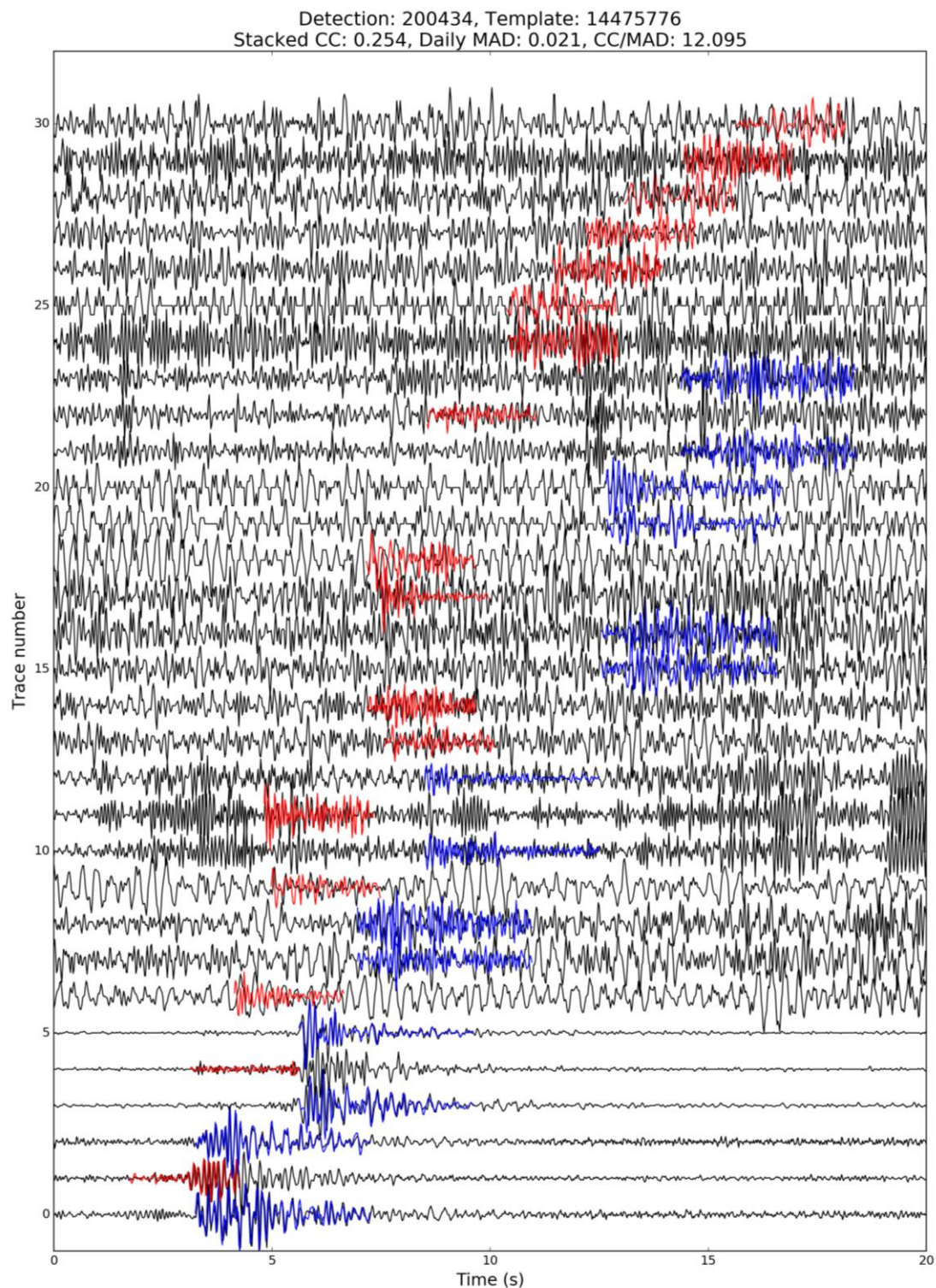


Fig. S2.

Example of an event detected with template matching. P-wave template waveforms are colored red, and S-wave template waveforms are colored blue. Note that not all stations have P and S template waveforms that meet the quality control criteria (Methods).

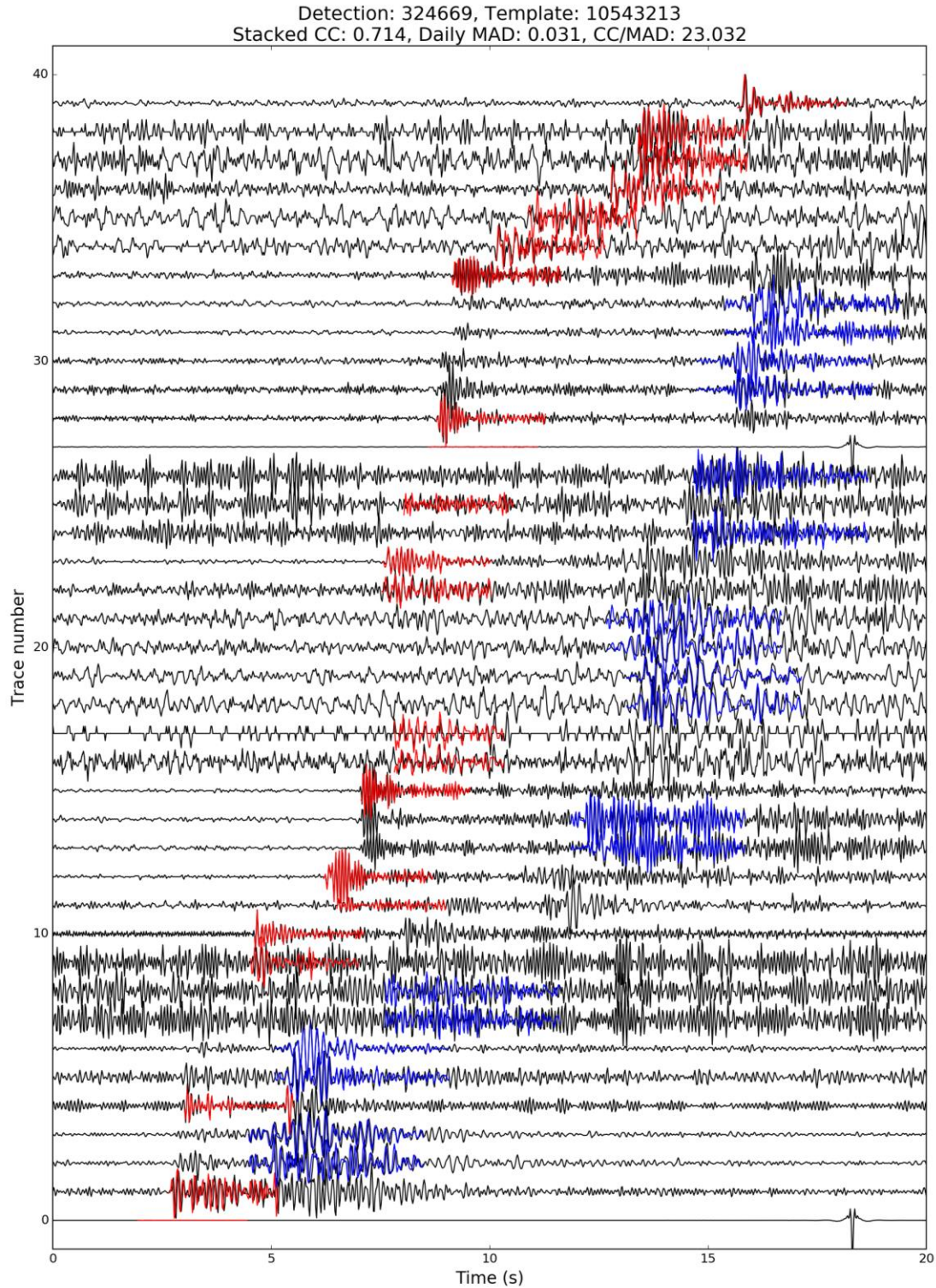


Fig. S3.

Example of an event detected with template matching. P-wave template waveforms are colored red, and S-wave template waveforms are colored blue. Note that not all stations have P and S template waveforms that meet the quality control criteria (Methods).

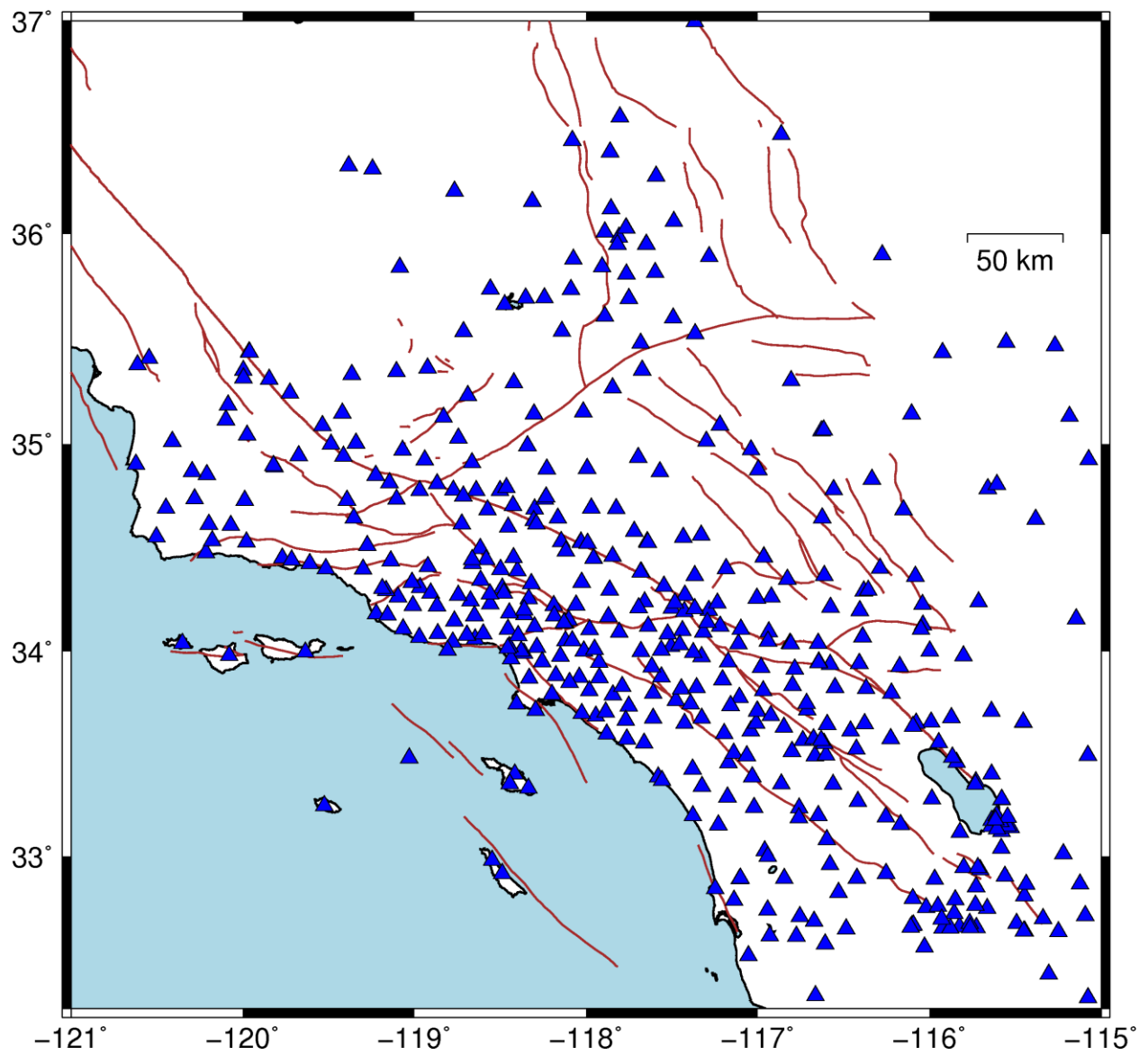


Fig. S4.

Map of station distribution used for the template matching and differential time measurements.

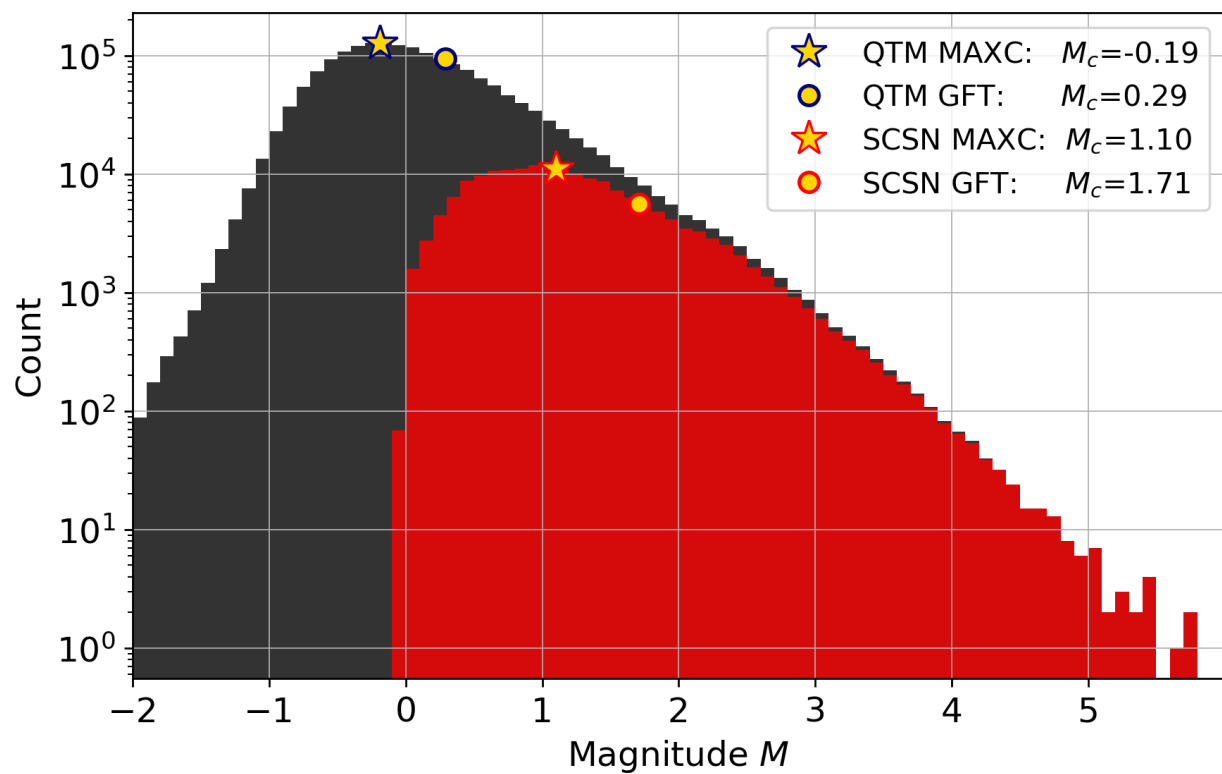


Fig. S5.

Magnitude of completeness (M_c) estimates and incremental magnitude distributions for the QTM and SCSN catalogs from 2008-2017. The preferred M_c estimates are obtained from the GFT method (circular markers), with the maximum curvature estimates (star markers) shown for comparison.

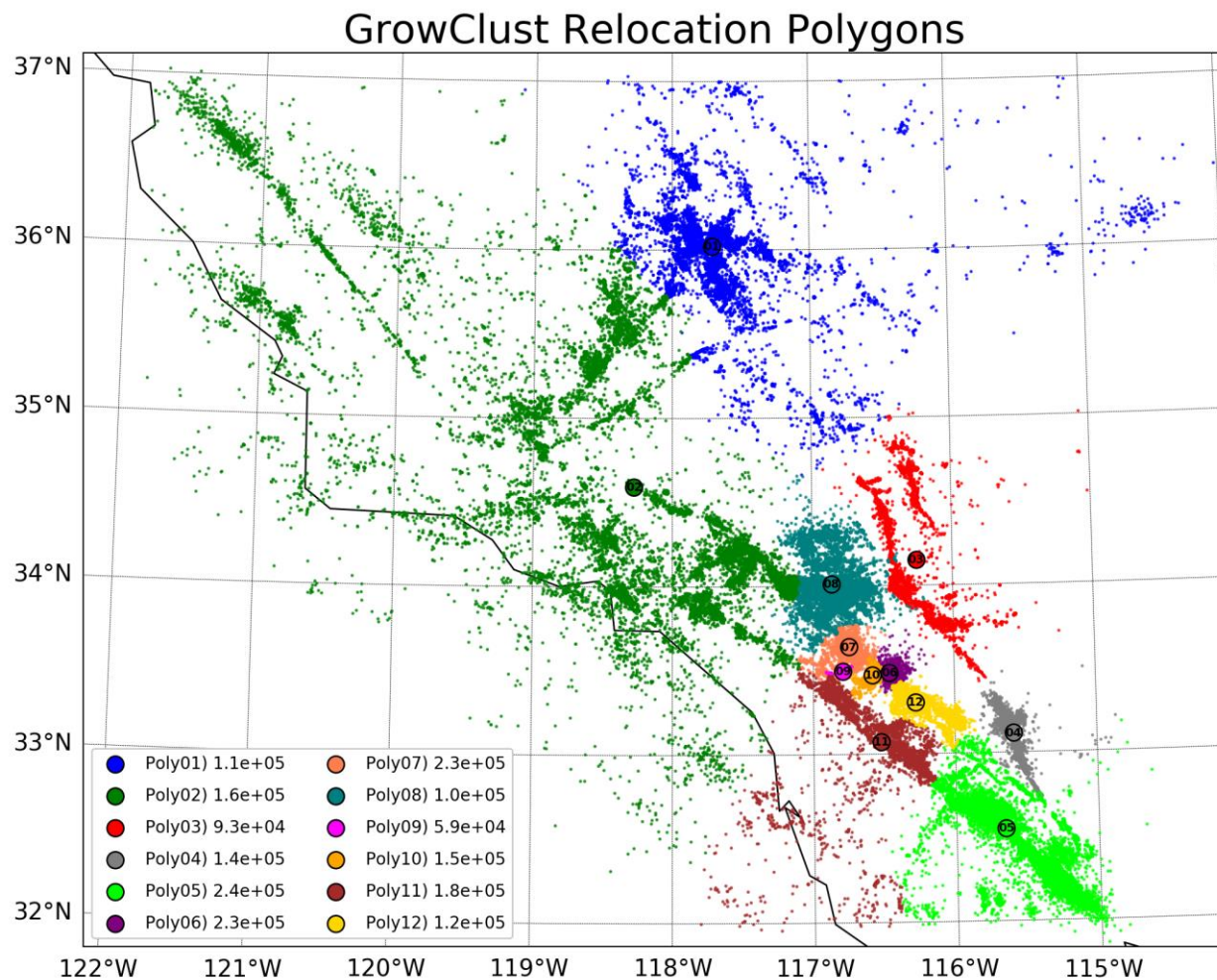


Fig. S6.

The 12 polygons used in GrowClust relative hypocentral relocation technique. The legend indicates the polygon number as well as the number of events assigned to it. During the relocation process, each of the polygons shown above are padded with additional events to ensure that each event assigned to a given polygon is relocated in tandem with its 200 nearest neighbors.

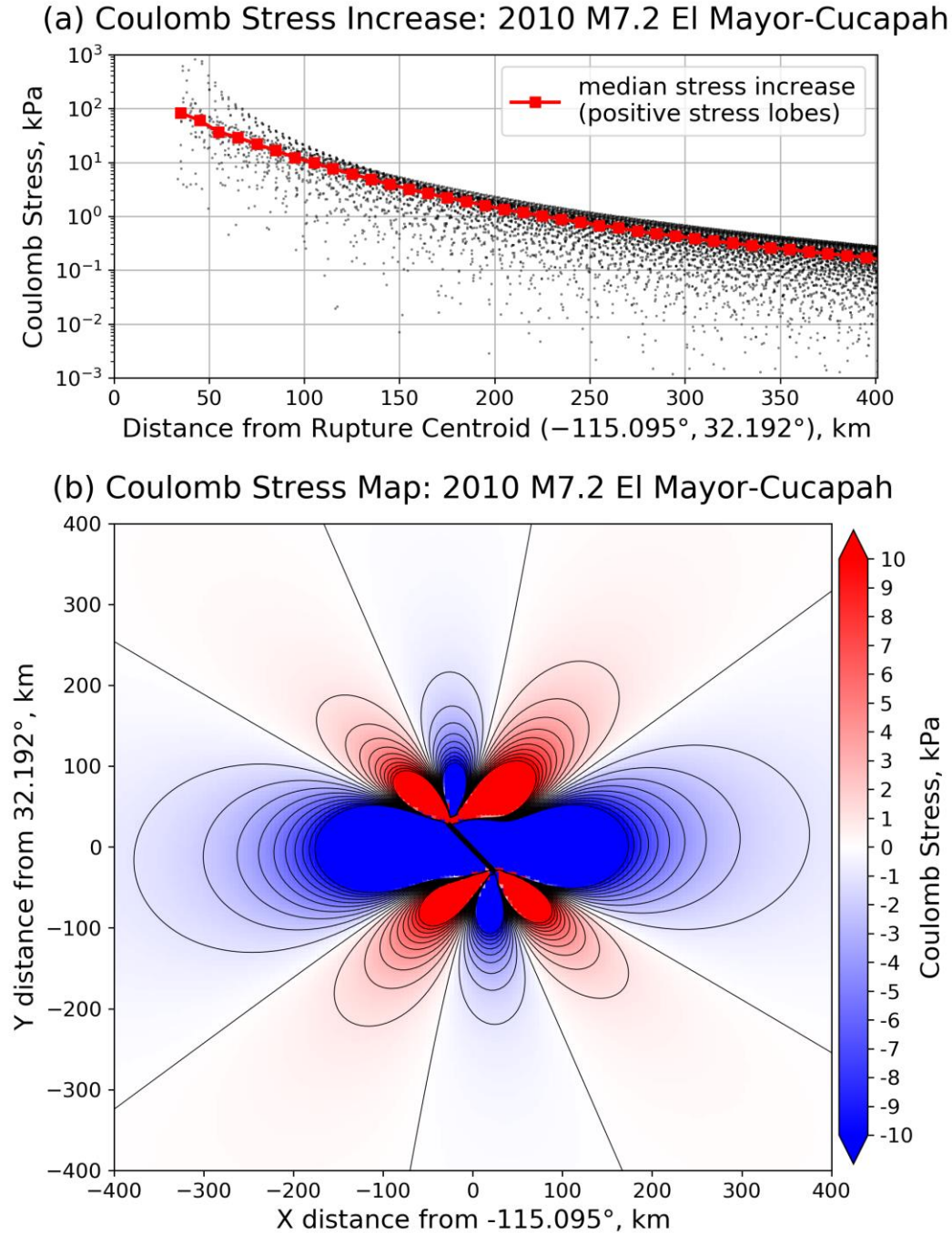


Fig. S7.

Coulomb stress change for the 2010 M7.2 El Mayor-Cucapah earthquake. Coulomb stress at 10km depth is calculated on a rectangular grid surrounding the mainshock centroid, assuming a uniform-slip rupture model and fault planes aligned with the mainshock rupture. (a) Coulomb stress increase as function of distance (black dots) for grid cells within the positively stressed regions, with the median stress increase denoted in red. (b) Map view of Coulomb stress change at 10km depth, with distance coordinates relative to the rupture centroid. Black contours correspond to 1kPa intervals.

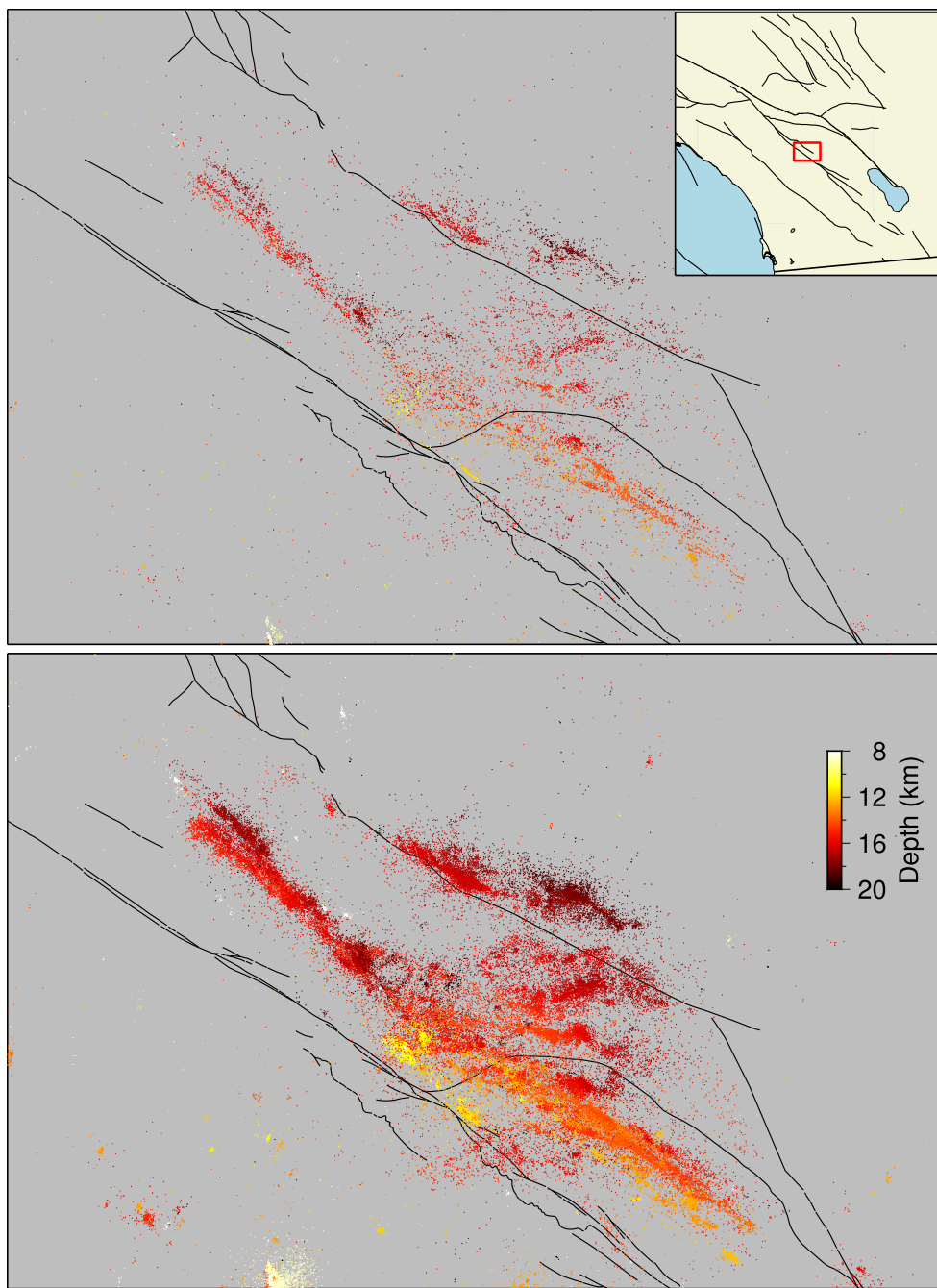


Fig. S8.

Seismicity in the Hot Springs section of the San Jacinto fault zone (see figure inset). The upper panel shows seismicity in the SCSN catalog, while the lower panel is from the QTM catalog.

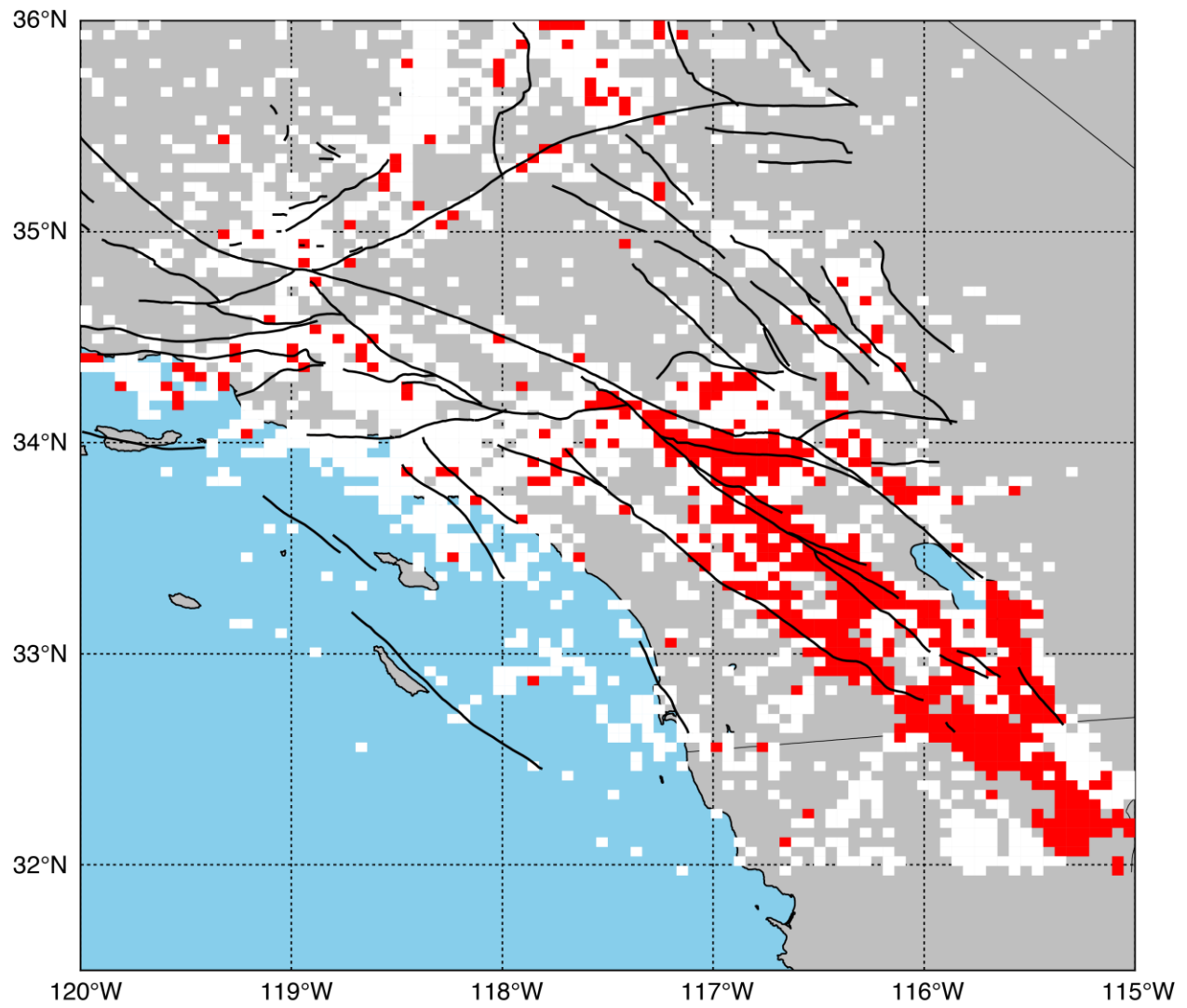


Fig. S9.
Similar analysis to Fig. 4A, but with a uniform minimum magnitude of 0.5 imposed across the dataset.

References and Notes

1. F. Omori, On the aftershocks of earthquakes. *Journal of the College of Science, Imperial University of Tokyo* **7**, 111–120 (1894).
2. C. F. Richter, An instrumental earthquake magnitude scale. *Bull. Seismol. Soc. Am.* **25**, 1–32 (1935).
3. B. Gutenberg, C. F. Richter, Frequency of earthquakes in California. *Bull. Seismol. Soc. Am.* **34**, 185–188 (1944).
4. P. M. Shearer, Parallel fault strands at 9-km depth resolved on the Imperial Fault, Southern California. *Geophys. Res. Lett.* **29**, 19-1–19-4 (2002). [doi:10.1029/2002GL015302](https://doi.org/10.1029/2002GL015302)
5. E. Fukuyama, W. L. Ellsworth, F. Waldhauser, A. Kubo, Detailed Fault Structure of the 2000 Western Tottori, Japan, Earthquake Sequence. *Bull. Seismol. Soc. Am.* **93**, 1468–1478 (2003). [doi:10.1785/0120020123](https://doi.org/10.1785/0120020123)
6. Z. E. Ross, E. Hauksson, Y. Ben-Zion, Abundant off-fault seismicity and orthogonal structures in the San Jacinto fault zone. *Sci. Adv.* **3**, e1601946 (2017). [doi:10.1126/sciadv.1601946](https://doi.org/10.1126/sciadv.1601946) [Medline](#)
7. R. B. Lohman, J. J. McGuire, Earthquake swarms driven by aseismic creep in the Salton Trough, California. *J. Geophys. Res. Solid Earth* **112**, B04405 (2007). [doi:10.1029/2006JB004596](https://doi.org/10.1029/2006JB004596)
8. D. R. Shelly, W. L. Ellsworth, D. P. Hill, Fluid-faulting evolution in high definition: Connecting fault structure and frequency-magnitude variations during the 2014 Long Valley Caldera, California, earthquake swarm. *J. Geophys. Res. Solid Earth* **121**, 1776–1795 (2016). [doi:10.1002/2015JB012719](https://doi.org/10.1002/2015JB012719)
9. J. Dieterich, A constitutive law for rate of earthquake production and its application to earthquake clustering. *J. Geophys. Res. Solid Earth* **99**, 2601–2618 (1994). [doi:10.1029/93JB02581](https://doi.org/10.1029/93JB02581)
10. E. S. Cochran, J. E. Vidale, S. Tanaka, Earth tides can trigger shallow thrust fault earthquakes. *Science* **306**, 1164–1166 (2004). [doi:10.1126/science.1103961](https://doi.org/10.1126/science.1103961) [Medline](#)
11. S. A. Miller, C. Collettini, L. Chiaraluce, M. Cocco, M. Barchi, B. J. P. Kaus, Aftershocks driven by a high-pressure CO₂ source at depth. *Nature* **427**, 724–727 (2004). [doi:10.1038/nature02251](https://doi.org/10.1038/nature02251) [Medline](#)
12. S. J. Gibbons, F. Ringdal, The detection of low magnitude seismic events using array-based waveform correlation. *Geophys. J. Int.* **165**, 149–166 (2006). [doi:10.1111/j.1365-246X.2006.02865.x](https://doi.org/10.1111/j.1365-246X.2006.02865.x)
13. D. R. Shelly, G. C. Beroza, S. Ide, Non-volcanic tremor and low-frequency earthquake swarms. *Nature* **446**, 305–307 (2007). [doi:10.1038/nature05666](https://doi.org/10.1038/nature05666) [Medline](#)
14. Z. Peng, P. Zhao, Migration of early aftershocks following the 2004 Parkfield earthquake. *Nat. Geosci.* **2**, 877–881 (2009). [doi:10.1038/ngeo697](https://doi.org/10.1038/ngeo697)
15. A. Kato, J. Fukuda, S. Nakagawa, K. Obara, Foreshock migration preceding the 2016 Mw 7.0 Kumamoto earthquake, Japan. *Geophys. Res. Lett.* **43**, 8945–8953 (2016). [doi:10.1002/2016GL070079](https://doi.org/10.1002/2016GL070079)

16. D. T. Trugman, P. M. Shearer, A Hierarchical Clustering Algorithm for Relative Earthquake Relocation, with Application to the Spanish Springs and Sheldon, Nevada, Earthquake Sequences. *Seismol. Res. Lett.* **88**, 379–391 (2017). [doi:10.1785/0220160188](https://doi.org/10.1785/0220160188)
17. E. Hauksson, W. Z. Yang, P. M. Shearer, Waveform Relocated Earthquake Catalog for Southern California (1981 to June 2011). *Bull. Seismol. Soc. Am.* **102**, 2239–2244 (2012). [doi:10.1785/0120120010](https://doi.org/10.1785/0120120010)
18. W. L. Ellsworth, F. Bulut, Nucleation of the 1999 Izmit earthquake by a triggered cascade of foreshocks. *Nat. Geosci.* **11**, 531–535 (2018). [doi:10.1038/s41561-018-0145-1](https://doi.org/10.1038/s41561-018-0145-1)
19. E. Hauksson, J. Stock, R. Bilham, M. Boese, X. Chen, E. J. Fielding, J. Galetzka, K. W. Hudnut, K. Hutton, L. M. Jones, H. Kanamori, P. M. Shearer, J. Steidl, J. Treiman, S. Wei, W. Yang, Report on the August 2012 Brawley Earthquake Swarm in Imperial Valley, Southern California. *Seismol. Res. Lett.* **84**, 177–189 (2013). [doi:10.1785/0220120169](https://doi.org/10.1785/0220120169)
20. S. Wei, J.-P. Avouac, K. W. Hudnut, A. Donnellan, J. W. Parker, R. W. Graves, D. Helmberger, E. Fielding, Z. Liu, F. Cappa, M. Eneva, The 2012 Brawley swarm triggered by injection-induced aseismic slip. *Earth Planet. Sci. Lett.* **422**, 115–125 (2015). [doi:10.1016/j.epsl.2015.03.054](https://doi.org/10.1016/j.epsl.2015.03.054)
21. R. S. Stein, The role of stress transfer in earthquake occurrence. *Nature* **402**, 605–609 (1999). [doi:10.1038/45144](https://doi.org/10.1038/45144)
22. K. R. Felzer, E. E. Brodsky, Decay of aftershock density with distance indicates triggering by dynamic stress. *Nature* **441**, 735–738 (2006). [doi:10.1038/nature04799](https://doi.org/10.1038/nature04799) [Medline](#)
23. D. P. Hill, P. A. Reasenberg, A. Michael, W. J. Arabaz, G. Beroza, D. Brumbaugh, J. N. Brune, R. Castro, S. Davis, D. Depolo, W. L. Ellsworth, J. Gomberg, S. Harmsen, L. House, S. M. Jackson, M. J. S. Johnston, L. Jones, R. Keller, S. Malone, L. Munguia, S. Nava, J. C. Pechmann, A. Sanford, R. W. Simpson, R. B. Smith, M. Stark, M. Stickney, A. Vidal, S. Walter, V. Wong, J. Zollweg, Seismicity remotely triggered by the magnitude 7.3 Landers, California, earthquake. *Science* **260**, 1617–1623 (1993). [doi:10.1126/science.260.5114.1617](https://doi.org/10.1126/science.260.5114.1617) [Medline](#)
24. D. Kilb, J. Gomberg, P. Bodin, Triggering of earthquake aftershocks by dynamic stresses. *Nature* **408**, 570–574 (2000). [doi:10.1038/35046046](https://doi.org/10.1038/35046046) [Medline](#)
25. J. Gomberg, P. A. Reasenberg, P. Bodin, R. A. Harris, Earthquake triggering by seismic waves following the Landers and Hector Mine earthquakes. *Nature* **411**, 462–466 (2001). [doi:10.1038/35078053](https://doi.org/10.1038/35078053) [Medline](#)
26. S. G. Prejean, D. P. Hill, E. E. Brodsky, S. E. Hough, M. J. S. Johnston, S. D. Malone, D. H. Oppenheimer, A. M. Pitt, K. B. Richards-Dinger, Remotely Triggered Seismicity on the United States West Coast following the Mw 7.9 Denali Fault Earthquake. *Bull. Seismol. Soc. Am.* **94**, S348–S359 (2004). [doi:10.1785/0120040610](https://doi.org/10.1785/0120040610)
27. S. J. Wei, E. Fielding, S. Leprince, A. Sladen, J.-P. Avouac, D. Helmberger, E. Hauksson, R. Chu, M. Simons, K. Hudnut, T. Herring, R. Briggs, Superficial simplicity of the 2010 El Mayor-Cucapah earthquake of Baja California in Mexico. *Nat. Geosci.* **4**, 615–618 (2011). [doi:10.1038/ngeo1213](https://doi.org/10.1038/ngeo1213)

28. Materials and methods are available as supplementary materials.

29. X. Meng, Z. Peng, Seismicity rate changes in the Salton Sea Geothermal Field and the San Jacinto Fault Zone after the 2010 Mw 7.2 El Mayor-Cucapah earthquake. *Geophys. J. Int.* **197**, 1750–1762 (2014). [doi:10.1093/gji/ggu085](https://doi.org/10.1093/gji/ggu085)
30. Z. E. Ross, C. Rollins, E. S. Cochran, E. Hauksson, J.-P. Avouac, Y. Ben-Zion, Aftershocks driven by afterslip and fluid pressure sweeping through a fault-fracture mesh. *Geophys. Res. Lett.* **44**, 8260–8267 (2017). [doi:10.1002/2017GL074634](https://doi.org/10.1002/2017GL074634)
31. W. Zhu, G. C. Beroza, PhaseNet: A deep-neural-network-based seismic arrival-time picking method. *Geophys. J. Int.* **216**, 261–273 (2019).
32. Z. E. Ross, M.-A. Meier, E. Hauksson, T. H. Heaton, Generalized Seismic Phase Detection with Deep Learning. *Bull. Seismol. Soc. Am.* **108**, 2894–2901 (2018). [doi:10.1785/0120180080](https://doi.org/10.1785/0120180080)
33. Data are available from the Southern California Seismic Network (<https://doi.org/10.7914/SN/CI>), operated by the California Institute of Technology and the United States Geological Survey.
34. The Southern California Earthquake Data Center (<https://doi.org/10.7909/C3WD3xH1>) is the archive of the Southern California Seismic Network.
35. A. Tarantola, *Inverse Problem Theory and Methods for Model Parameter Estimation* (SIAM, 2005).
36. S. Wiemer, M. Wyss, Minimum Magnitude of Completeness in Earthquake Catalogs: Examples from Alaska, the Western United States, and Japan. *Bull. Seismol. Soc. Am.* **90**, 859–869 (2000). [doi:10.1785/0119990114](https://doi.org/10.1785/0119990114)
37. A. Mignan, J. Woessner, “Estimating the magnitude of completeness for earthquake catalogs,” *Community Online Resource for Statistical Seismicity Analysis* (2012); <https://doi.org/10.5078/corssa-00180805>.
38. B. Bender, Maximum likelihood estimation of b values for magnitude grouped data. *Bull. Seismol. Soc. Am.* **73**, 831–851 (1983).
39. E. Hauksson, Crustal structure and seismicity distribution adjacent to the Pacific and North America plate boundary in southern California. *J. Geophys. Res.* **105** (B6), 13875–13903 (2000). [doi:10.1029/2000JB900016](https://doi.org/10.1029/2000JB900016)
40. A. Y. Ng, M. I. Jordan, Y. Weiss, in *Advances in Neural Information Processing Systems* (MIT Press, 2001), pp. 849–856.
41. S. Toda, R. S. Stein, V. Sevilgen, J. Lin, Coulomb 3.3 Graphic-Rich Deformation and Stress-Change Software for Earthquake, Tectonic, and Volcano Research and Teaching–User Guide. *U.S. Geological Survey Open-File Report*. **2011–1060** (2011) (available at <https://pubs.usgs.gov/of/2011/1060/>).
42. M. Huang, E. J. Fielding, H. Dickinson, J. Sun, J. A. Gonzalez-Ortega, A. M. Freed, R. Bürgmann, Fault geometry inversion and slip distribution of the 2010 Mw 7.2 El Mayor-Cucapah earthquake from geodetic data. *J. Geophys. Res. Solid Earth* **122**, 607–621 (2017). [doi:10.1002/2016JB012858](https://doi.org/10.1002/2016JB012858)